

**Cross section and longitudinal single-spin asymmetry A_L for forward
 $W^\pm \rightarrow \mu^\pm \nu$ production in polarized $p + p$ collisions at $\sqrt{s} = 510$ GeV**

A. Adare,¹³ C. Aidala,^{39,44} N. N. Ajitanand,^{62,*} Y. Akiba,^{57,58,†} R. Akimoto,¹² J. Alexander,⁶² M. Alfred,²⁴ K. Aoki,^{32,57} N. Apadula,^{29,63} Y. Aramaki,⁵⁷ H. Asano,^{35,57} E. T. Atomssa,⁶³ T. C. Awes,⁵³ B. Azmoun,⁷ V. Babintsev,²⁵ A. Bagoly,¹⁷ M. Bai,⁶ X. Bai,¹¹ N. S. Bandara,⁴³ B. Bannier,⁶³ K. N. Barish,⁸ S. Bathe,^{5,58} V. Baublis,⁵⁶ C. Baumann,⁷ S. Baumgart,⁵⁷ A. Bazilevsky,⁷ M. Beaumier,⁸ S. Beckman,¹³ R. Belmont,^{13,44,68} A. Berdnikov,⁶⁰ Y. Berdnikov,⁶⁰ D. Black,⁸ D. S. Blau,^{34,49} M. Boer,³⁹ J. S. Bok,⁵¹ K. Boyle,⁵⁸ M. L. Brooks,³⁹ J. Bryslawskyj,^{5,8} H. Buesching,⁷ V. Bumazhnov,²⁵ S. Butsyk,⁵⁰ S. Campbell,^{14,29} V. Canoa Roman,⁶³ C.-H. Chen,⁵⁸ C. Y. Chi,¹⁴ M. Chiu,^{7,26} I. J. Choi,²⁶ J. B. Choi,^{10,*} S. Choi,⁶¹ P. Christiansen,⁴⁰ T. Chujo,⁶⁷ V. Cianciolo,⁵³ Z. Citron,⁶⁹ B. A. Cole,¹⁴ M. Connors,^{21,58} N. Cronin,^{45,63} N. Crossette,⁴⁵ M. Csanad,¹⁷ T. Csorgo,^{18,70} T. W. Danley,⁵² A. Datta,⁵⁰ M. S. Daugherity,¹ G. David,^{7,63} K. DeBlasio,⁵⁰ K. Dehmelt,⁶³ A. Denisov,²⁵ A. Deshpande,^{58,63} E. J. Desmond,⁷ L. Ding,²⁹ A. Dion,⁶³ J. H. Do,⁷¹ L. D’Orazio,⁴² O. Drapier,³⁶ A. Drees,⁶³ K. A. Drees,⁷ J. M. Durham,³⁹ A. Durum,²⁵ T. Engelmore,¹⁴ A. Enokizono,^{57,59} H. En’yo,^{57,58} S. Esumi,⁶⁷ K. O. Eyser,⁷ B. Fadem,⁴⁵ W. Fan,⁶³ N. Feege,⁶³ D. E. Fields,⁵⁰ M. Finger,⁹ M. Finger, Jr.,⁹ F. Fleuret,³⁶ S. L. Fokin,³⁴ J. E. Frantz,⁵² A. Franz,⁷ A. D. Frawley,²⁰ Y. Fukao,³² T. Fusayasu,⁴⁷ K. Gainey,¹ C. Gal,⁶³ P. Gallus,¹⁵ P. Garg,^{3,63} A. Garishvili,⁶⁵ I. Garishvili,³⁸ H. Ge,⁶³ F. Giordano,²⁶ A. Glenn,³⁸ X. Gong,⁶² M. Gonin,³⁶ Y. Goto,^{57,58} R. Granier de Cassagnac,³⁶ N. Grau,² S. V. Greene,⁶⁸ M. Grosse Perdekamp,²⁶ Y. Gu,⁶² T. Gunji,¹² H. Guragain,²¹ T. Hachiya,^{57,58} J. S. Haggerty,⁷ K. I. Hahn,¹⁹ H. Hamagaki,¹² S. Y. Han,¹⁹ J. Hanks,⁶³ S. Hasegawa,³⁰ T. O. S. Haseler,²¹ K. Hashimoto,^{57,59} R. Hayano,¹² X. He,²¹ T. K. Hemmick,⁶³ T. Hester,⁸ J. C. Hill,²⁹ K. Hill,¹³ A. Hodges,²¹ R. S. Hollis,⁸ K. Homma,²³ B. Hong,³³ T. Hoshino,²³ N. Hotvedt,²⁹ J. Huang,^{7,39} S. Huang,⁶⁸ T. Ichihara,⁵⁷ Y. Ikeda,⁵⁷ K. Imai,³⁰ Y. Imazu,⁵⁷ M. Inaba,⁶⁷ A. Iordanova,⁸ D. Isenhower,¹ A. Isinhue,⁴⁵ D. Ivanishchev,⁵⁶ B. V. Jacak,⁶³ S. J. Jeon,⁴⁶ M. Jezghani,²¹ Z. Ji,⁶³ J. Jia,^{7,62} X. Jiang,³⁹ B. M. Johnson,^{7,21} E. Joo,³³ K. S. Joo,⁴⁶ D. Jouan,⁵⁴ D. S. Jumper,²⁶ J. Kamin,⁶³ S. Kanda,^{12,32,57} B. H. Kang,²² J. H. Kang,⁷¹ J. S. Kang,²² J. Kapustinsky,³⁹ D. Kawall,⁴³ A. V. Kazantsev,³⁴ J. A. Key,⁵⁰ V. Khachatryan,⁶³ P. K. Khandai,³ A. Khanzadeev,⁵⁶ K. Kihara,⁶⁷ K. M. Kijima,²³ C. Kim,³³ D. H. Kim,¹⁹ D. J. Kim,³¹ E.-J. Kim,¹⁰ H.-J. Kim,⁷¹ M. Kim,⁶¹ Y.-J. Kim,²⁶ Y. K. Kim,²² D. Kincses,¹⁷ E. Kistenev,⁷ J. Klatsky,²⁰ D. Kleinjan,⁸ P. Kline,⁶³ T. Koblesky,¹³ M. Kofarago,^{17,70} B. Komkov,⁵⁶ J. Koster,^{26,58} D. Kotchetkov,⁵² D. Kotov,^{56,60} F. Krizek,³¹ K. Kurita,⁵⁹ M. Kurosawa,^{57,58} Y. Kwon,⁷¹ R. Lacey,⁶² Y. S. Lai,¹⁴ J. G. Lajoie,²⁹ A. Lebedev,²⁹ D. M. Lee,³⁹ G. H. Lee,¹⁰ J. Lee,^{19,64} K. B. Lee,³⁹ K. S. Lee,³³ S. H. Lee,^{29,63} M. J. Leitch,³⁹ M. Leitgab,²⁶ Y. H. Leung,⁶³ B. Lewis,⁶³ N. A. Lewis,⁴⁴ X. Li,¹¹ X. Li,³⁹ S. H. Lim,^{39,71} M. X. Liu,³⁹ S. Lokos,^{17,18} D. Lynch,⁷ C. F. Maguire,⁶⁸ T. Majoros,¹⁶ Y. I. Makdisi,⁶ M. Makek,^{69,72} A. Manion,⁶³ V. I. Manko,³⁴ E. Mannel,⁷ M. McCumber,^{13,39} P. L. McGaughey,³⁹ D. McGlinchey,^{13,20,39} C. McKinney,²⁶ A. Meles,⁵¹ M. Mendoza,⁸ B. Meredith,^{14,26} Y. Miake,⁶⁷ T. Mibe,³² A. C. Mignerey,⁴² D. E. Mihalik,⁶³ A. J. Miller,¹ A. Milov,⁶⁹ D. K. Mishra,⁴ J. T. Mitchell,⁷ G. Mitsuka,⁵⁸ S. Miyasaka,^{57,66} S. Mizuno,^{57,67} A. K. Mohanty,⁴ S. Mohapatra,⁶² P. Montuenga,²⁶ T. Moon,⁷¹ D. P. Morrison,⁷ S. I. Morrow,⁶⁸ M. Moskowitz,⁴⁵ T. V. Moukhanova,³⁴ T. Murakami,^{35,57} J. Murata,^{57,59} A. Mwai,⁶² T. Nagae,³⁵ S. Nagamiya,^{32,57} K. Nagashima,²³ J. L. Nagle,¹³ M. I. Nagy,¹⁷ I. Nakagawa,^{57,58} H. Nakagomi,^{57,67} Y. Nakamiya,²³ K. R. Nakamura,^{35,57} T. Nakamura,⁵⁷ K. Nakano,^{57,66} C. Natrass,⁶⁵ P. K. Netrakanti,⁴ M. Nihashi,^{23,57} T. Niida,⁶⁷ R. Nouicer,^{7,58} T. Novak,^{18,70} N. Novitzky,^{31,63} A. S. Nyanin,³⁴ E. O’Brien,⁷ C. A. Ogilvie,²⁹ H. Oide,¹² K. Okada,⁵⁸ J. D. Orjuela Koop,¹³ J. D. Osborn,⁴⁴ A. Oskarsson,⁴⁰ K. Ozawa,^{32,67} R. Pak,⁷ V. Pantuev,²⁷ V. Papavassiliou,⁵¹ I. H. Park,^{19,64} S. Park,^{57,61,63} S. K. Park,³³ S. F. Pate,⁵¹ L. Patel,²¹ M. Patel,²⁹ J.-C. Peng,²⁶ W. Peng,⁶⁸ D. V. Perepelitsa,^{7,13,14} G. D. N. Perera,⁵¹ D. Yu. Peressounko,³⁴ C. E. PerezLara,⁶³ J. Perry,²⁹ R. Petti,^{7,63} C. Pinkenburg,⁷ R. Pinson,¹ R. P. Pisani,⁷ M. L. Purschke,⁷ H. Qu,¹ P. V. Radzevich,⁶⁰ J. Rak,³¹ I. Ravinovich,⁶⁹ K. F. Read,^{53,65} D. Reynolds,⁶² V. Riabov,^{49,56} Y. Riabov,^{56,60} E. Richardson,⁴² D. Richford,⁵ T. Rinn,²⁹ N. Rivelis,⁵² D. Roach,⁶⁸ S. D. Rolnick,⁸ M. Rosati,²⁹ Z. Rowan,⁵ J. G. Rubin,⁴⁴ J. Runchey,²⁹ M. S. Ryu,²² B. Sahlmueller,⁶³ N. Saito,³² T. Sakaguchi,⁷ H. Sako,³⁰ V. Samsonov,^{49,56} M. Sarsour,²¹ S. Sato,³⁰ S. Sawada,³² B. Schaefer,⁶⁸ B. K. Schmoll,⁶⁵ K. Sedgwick,⁸ J. Seele,⁵⁸ R. Seidl,^{26,57,58} Y. Sekiguchi,¹² A. Sen,^{21,29,65} R. Seto,⁸ P. Sett,⁴ A. Sexton,⁴² D. Sharma,⁶³ A. Shaver,²⁹ I. Shein,²⁵ T.-A. Shibata,^{57,66} K. Shigaki,²³ M. Shimomura,^{29,48} K. Shoji,⁵⁷ P. Shukla,⁴ A. Sickles,^{7,26} C. L. Silva,³⁹ D. Silvermyr,^{40,53} B. K. Singh,³ C. P. Singh,³ V. Singh,³ M. J. Skoby,⁴⁴ M. Skolnik,⁴⁵ M. Slunecka,⁹ S. Solano,⁴⁵ R. A. Soltz,³⁸ W. E. Sondheim,³⁹ S. P. Sorensen,⁶⁵ I. V. Sourikova,⁷ P. W. Stankus,⁵³ P. Steinberg,⁷ E. Stenlund,⁴⁰ M. Stepanov,^{43,*} A. Ster,⁷⁰ S. P. Stoll,⁷ M. R. Stone,¹³ T. Sugitate,²³ A. Sukhanov,⁷ T. Sumita,⁵⁷ J. Sun,⁶³ Z. Sun,¹⁶ J. Sziklai,⁷⁰ A. Takahara,¹² A. Taketani,^{57,58} Y. Tanaka,⁴⁷ K. Tanida,^{30,58,61} M. J. Tannenbaum,⁷ S. Tarafdar,^{3,68,69} A. Taranenko,^{49,62} E. Tenant,⁵¹ R. Tieulent,⁴¹ A. Timilsina,²⁹ T. Todoroki,^{57,67} M. Tomasek,^{15,28} H. Torii,¹² M. Towell,¹ R. Towell,¹ R. S. Towell,¹ I. Tserruya,⁶⁹ B. Ujvari,¹⁶ H. W. van Hecke,³⁹ M. Vargyas,^{17,70} E. Vazquez-Zambrano,¹⁴ A. Veicht,¹⁴ J. Velkovska,⁶⁸ R. Vertesi,⁷⁰ M. Virius,¹⁵ A. Vossen,²⁶ V. Vrba,^{15,28} E. Vznuzdaev,⁵⁶ X. R. Wang,^{51,58} D. Watanabe,²³ K. Watanabe,^{57,59} Y. Watanabe,^{57,58} Y. S. Watanabe,^{12,32} F. Wei,⁵¹ S. Whitaker,²⁹ S. Wolin,²⁶ C. P. Wong,²¹

C. L. Woody,⁷ M. Wysocki,⁵³ B. Xia,⁵² C. Xu,⁵¹ Q. Xu,⁶⁸ L. Xue,²¹ S. Yalcin,⁶³ Y. L. Yamaguchi,^{12,58,63} R. Yang,²⁶ A. Yanovich,²⁵ S. Yokkaichi,^{57,58} J. H. Yoo,³³ I. Yoon,⁶¹ Z. You,³⁹ I. Younus,^{37,50} H. Yu,^{51,55} I. E. Yushmanov,³⁴ W. A. Zajc,¹⁴ A. Zelenski,⁶ S. Zharko,⁶⁰ S. Zhou,¹¹ and L. Zou⁸

(PHENIX Collaboration)

¹Abilene Christian University, Abilene, Texas 79699, USA

²Department of Physics, Augustana University, Sioux Falls, South Dakota 57197, USA

³Department of Physics, Banaras Hindu University, Varanasi 221005, India

⁴Bhabha Atomic Research Centre, Bombay 400 085, India

⁵Baruch College, City University of New York, New York, New York 10010 USA

⁶Collider-Accelerator Department, Brookhaven National Laboratory, Upton, New York 11973-5000, USA

⁷Physics Department, Brookhaven National Laboratory, Upton, New York 11973-5000, USA

⁸University of California-Riverside, Riverside, California 92521, USA

⁹Charles University, Ovocný trh 5, Praha 1, 116 36 Prague, Czech Republic

¹⁰Chonbuk National University, Jeonju 561-756, Korea

¹¹Science and Technology on Nuclear Data Laboratory, China Institute of Atomic Energy, Beijing 102413, People's Republic of China

¹²Center for Nuclear Study, Graduate School of Science, University of Tokyo, 7-3-1 Hongo, Bunkyo, Tokyo 113-0033, Japan

¹³University of Colorado, Boulder, Colorado 80309, USA

¹⁴Columbia University, New York, New York 10027, USA and Nevis Laboratories, Irvington, New York 10533, USA

¹⁵Czech Technical University, Zikova 4, 166 36 Prague 6, Czech Republic

¹⁶Debrecen University, H-4010 Debrecen, Egyetem tér 1, Hungary

¹⁷ELTE, Eötvös Loránd University, H-1117 Budapest, Pázmány P. s. 1/A, Hungary

¹⁸Eszterházy Károly University, Károly Róbert Campus, H-3200 Gyöngyös, Mátrai út 36, Hungary

¹⁹Ewha Womans University, Seoul 120-750, Korea

²⁰Florida State University, Tallahassee, Florida 32306, USA

²¹Georgia State University, Atlanta, Georgia 30303, USA

²²Hanyang University, Seoul 133-792, Korea

²³Hiroshima University, Kagamiyama, Higashi-Hiroshima 739-8526, Japan

²⁴Department of Physics and Astronomy, Howard University, Washington, D.C. 20059, USA

²⁵IHEP Protvino, State Research Center of Russian Federation, Institute for High Energy Physics, Protvino 142281, Russia

²⁶University of Illinois at Urbana-Champaign, Urbana, Illinois 61801, USA

²⁷Institute for Nuclear Research of the Russian Academy of Sciences,

prospekt 60-letiya Oktyabrya 7a, Moscow 117312, Russia

²⁸Institute of Physics, Academy of Sciences of the Czech Republic,

Na Slovance 2, 182 21 Prague 8, Czech Republic

²⁹Iowa State University, Ames, Iowa 50011, USA

³⁰Advanced Science Research Center, Japan Atomic Energy Agency,

2-4 Shirakata Shirane, Tokai-mura, Naka-gun, Ibaraki-ken 319-1195, Japan

³¹Helsinki Institute of Physics and University of Jyväskylä, P.O. Box 35, FI-40014 Jyväskylä, Finland

³²KEK, High Energy Accelerator Research Organization, Tsukuba, Ibaraki 305-0801, Japan

³³Korea University, Seoul 136-701, Korea

³⁴National Research Center "Kurchatov Institute", Moscow 123098, Russia

³⁵Kyoto University, Kyoto 606-8502, Japan

³⁶Laboratoire Leprince-Ringuet, Ecole Polytechnique, CNRS-IN2P3,

Route de Saclay, F-91128 Palaiseau, France

³⁷Physics Department, Lahore University of Management Sciences, Lahore 54792, Pakistan

³⁸Lawrence Livermore National Laboratory, Livermore, California 94550, USA

³⁹Los Alamos National Laboratory, Los Alamos, New Mexico 87545, USA

⁴⁰Department of Physics, Lund University, Box 118, SE-221 00 Lund, Sweden

⁴¹IPNL, CNRS/IN2P3, University Lyon, Université Lyon 1, F-69622 Villeurbanne, France

⁴²University of Maryland, College Park, Maryland 20742, USA

⁴³Department of Physics, University of Massachusetts, Amherst, Massachusetts 01003-9337, USA

⁴⁴Department of Physics, University of Michigan, Ann Arbor, Michigan 48109-1040, USA

⁴⁵Muhlenberg College, Allentown, Pennsylvania 18104-5586, USA

⁴⁶*Myongji University, Yongin, Kyonggido 449-728, Korea*

⁴⁷*Nagasaki Institute of Applied Science, Nagasaki-shi, Nagasaki 851-0193, Japan*

⁴⁸*Nara Women's University, Kita-uoya Nishi-machi Nara 630-8506, Japan*

⁴⁹*National Research Nuclear University, MEPhI, Moscow Engineering Physics Institute, Moscow 115409, Russia*

⁵⁰*University of New Mexico, Albuquerque, New Mexico 87131, USA*

⁵¹*New Mexico State University, Las Cruces, New Mexico 88003, USA*

⁵²*Department of Physics and Astronomy, Ohio University, Athens, Ohio 45701, USA*

⁵³*Oak Ridge National Laboratory, Oak Ridge, Tennessee 37831, USA*

⁵⁴*IPN-Orsay, Université Paris-Sud, CNRS/IN2P3, Université Paris-Saclay, BP1, F-91406 Orsay, France*

⁵⁵*Peking University, Beijing 100871, People's Republic of China*

⁵⁶*PNPI, Petersburg Nuclear Physics Institute, Gatchina, Leningrad region 188300, Russia*

⁵⁷*RIKEN Nishina Center for Accelerator-Based Science, Wako, Saitama 351-0198, Japan*

⁵⁸*RIKEN BNL Research Center, Brookhaven National Laboratory, Upton, New York 11973-5000, USA*

⁵⁹*Physics Department, Rikkyo University, 3-34-1 Nishi-Ikebukuro, Toshima, Tokyo 171-8501, Japan*

⁶⁰*Saint Petersburg State Polytechnic University, Saint Petersburg, 195251 Russia*

⁶¹*Department of Physics and Astronomy, Seoul National University, Seoul 151-742, Korea*

⁶²*Chemistry Department, Stony Brook University, SUNY, Stony Brook, New York 11794-3400, USA*

⁶³*Department of Physics and Astronomy, Stony Brook University, SUNY, Stony Brook, New York 11794-3800, USA*

⁶⁴*Sungkyunkwan University, Suwon 440-746, Korea*

⁶⁵*University of Tennessee, Knoxville, Tennessee 37996, USA*

⁶⁶*Department of Physics, Tokyo Institute of Technology, Oh-okayama, Meguro, Tokyo 152-8551, Japan*

⁶⁷*Tomonaga Center for the History of the Universe, University of Tsukuba, Tsukuba, Ibaraki 305, Japan*

⁶⁸*Vanderbilt University, Nashville, Tennessee 37235, USA*

⁶⁹*Weizmann Institute, Rehovot 76100, Israel*

⁷⁰*Institute for Particle and Nuclear Physics, Wigner Research Centre for Physics, Hungarian Academy of Sciences (Wigner RCP, RMKI) H-1525 Budapest 114, P.O. Box 49, Budapest, Hungary*

⁷¹*Yonsei University, IPAP, Seoul 120-749, Korea*

⁷²*Department of Physics, Faculty of Science, University of Zagreb, Bijenička cesta 32 HR-10002 Zagreb, Croatia*



(Received 13 April 2018; published 14 August 2018)

We have measured the cross section and single-spin asymmetries from forward $W^\pm \rightarrow \mu^\pm \nu$ production in longitudinally polarized $p + p$ collisions at $\sqrt{s} = 510$ GeV using the PHENIX detector at the Relativistic Heavy Ion Collider. The cross sections are consistent with previous measurements at this collision energy, while the most forward and backward longitudinal single spin asymmetries provide new insights into the sea quark helicities in the proton. The charge of the W bosons provides a natural flavor separation of the participating partons.

DOI: 10.1103/PhysRevD.98.032007

I. INTRODUCTION

The spin of the proton and its decomposition is fundamentally important. Understanding its origin is essential to explaining how the strong interaction, described by quantum chromodynamics (QCD), creates

the basic building blocks of the visible matter in our universe, protons, and neutrons. Mostly from deep inelastic scattering measurements and hadron-hadron collisions, it is known that quarks and gluons make roughly equal contributions to the total momentum of the proton in the Bjorken frame [1–3]. Just like gluons, sea quarks also play a substantial role in the composition of the proton momentum. Unlike what is naively expected from gluon splitting, the unpolarized light quark sea is found to be asymmetric with more antidown quarks than antiup quarks at small to intermediate Bjorken $x < 0.2$, where x is the parton momentum fraction in the infinite momentum frame. See, for example, a review of the

^{*}Deceased.

[†]PHENIX Spokesperson: akiba@rcf.rhic.bnl.gov

Published by the American Physical Society under the terms of the [Creative Commons Attribution 4.0 International license](#). Further distribution of this work must maintain attribution to the author(s) and the published article's title, journal citation, and DOI. Funded by SCOAP³.

world data on the unpolarized light sea and the theoretical models related to it [4].

While several models can describe correctly the measured unpolarized light sea, these models differ significantly in their predictions for the polarized case [4]. Valence quark helicity contributions to the total spin of the nucleon are already relatively well known from deep inelastic scattering (DIS) and semi-inclusive DIS measurements. The gluon helicity contribution has very recently been found to also be nonzero [5–7], but sea quark helicities are still poorly understood. One of the main reasons is that DIS predominantly probes valence objects at the currently measured scales and x ranges. Second, the uncertainties of fragmentation functions in semi-inclusive measurements, needed to disentangle different flavors, dominate the existing sea quark helicity extractions. An elegant alternative to access sea quark helicities is via the weak interaction. Such processes are possible at the high scales proposed at a polarized electron-ion collider [8] or currently in polarized $p + p$ collisions at the Relativistic Heavy Ion Collider (RHIC) [9]. In $p + p$ collisions, real W 's can be produced in the annihilation of predominantly up and antidown quark pairs for W^+ production and down and antiup quark pairs for W^- production (if one neglects the small off-diagonal Cabibbo-Kobayashi-Masukawa matrix elements). Furthermore, the helicity of participating quarks and antiquarks is fixed to be left-handed and right-handed, respectively, due to the parity violating nature of the weak interaction. If one of the two proton beams is longitudinally polarized, the helicity of the proton beam therefore selects quarks that are polarized parallel or antiparallel with it and vice versa for antiquarks. Building the difference of the W production cross sections for positive and negative helicities normalized by their sum, one arrives at the single longitudinal spin asymmetry,

$$A_L^{pp \rightarrow W^+} \approx \frac{\Delta \bar{d}(x_1, Q) u(x_2, Q) - \Delta u(x_1, Q) \bar{d}(x_2, Q)}{\bar{d}(x_1, Q) u(x_2, Q) + u(x_1, Q) \bar{d}(x_2, Q)}, \quad (1)$$

in terms of the unpolarized parton distribution functions (PDFs) for up and antidown quarks, $u(x, Q)$ and $\bar{d}(x, Q)$, and their respective helicity PDFs $\Delta u(x, Q)$ and $\Delta \bar{d}(x, Q)$. The corresponding single spin asymmetry for W^- production becomes

$$A_L^{pp \rightarrow W^-} \approx \frac{\Delta \bar{u}(x_1, Q) d(x_2, Q) - \Delta d(x_1, Q) \bar{u}(x_2, Q)}{\bar{u}(x_1, Q) d(x_2, Q) + d(x_1, Q) \bar{u}(x_2, Q)}. \quad (2)$$

It accesses the other combination of light quark flavors. While the W production cross section is relatively low compared to strong processes, the scale is set by the mass of the produced W 's. Furthermore, no uncertainties due to fragmentation functions enter the interpretation of these single spin asymmetry measurements.

In the PHENIX experiment [10], W 's are not reconstructed kinematically themselves, but their leptonic decays ($W \rightarrow l \bar{\nu}_l$) are measured inclusively by detecting the charged decay lepton l only. At central rapidities, W decay electrons are reconstructed, while at forward rapidities ($1.1 < |\eta| < 2.6$ and $1.1 < |\eta| < 2.5$ for the north and south muon arms, respectively) decay muons are being studied. Recent results by STAR [11] and PHENIX [12,13] for the electron channels exist. In this paper, the first asymmetry measurement using muons and at forward/backward rapidities is reported.

In this analysis, we rely solely on the reconstruction of forward-going muons impinging the muon-spectrometer as the nonhermetic coverage of the PHENIX detector precludes a missing energy analysis to measure the neutrino. Although approximately half of the energy of the W is carried by the muon, only a small Jacobian peak is expected in the forward region, in contrast to earlier measurements at midrapidity. The reason is the additional longitudinal momentum which takes up a substantial part of the W decay muon's energy, as well as any nonzero initial W momentum. The very different kinematic regimes for central and forward W decay muons and respective yields are illustrated in Fig. 1 based on PYTHIA-6 simulations [14]. Furthermore, any remnant Jacobian peak is completely washed out by the limited momentum resolution of the muon spectrometer at large momenta. Consequently, a data-driven approach has been employed to identify the contributions by the various backgrounds in the data sample to extract W production cross sections and the corresponding single spin asymmetries. It should be noted that at forward rapidities, higher/lower x of around 0.3/0.1 from the forward/backward going proton can be probed in comparison to more central rapidities where both x are around 0.2. For W^- decays, the forward region also cleanly separates the down and antiup quark contributions by the forward/backward going protons while for W^+ decays a mixture of up and antidown quarks always contributes although at rather different x .

This paper is organized as follows: In Sec. II, the different data taking periods and the corresponding data sets are discussed including a brief description of the relevant detector systems and Monte Carlo sets used. Section III describes the initial event selection criteria used to screen the raw data for events with a high likelihood of containing W decay muons. In Sec. IV, the extraction of the actual signal, the W production cross section and the asymmetries are discussed before discussing the systematic studies in Sec. V. The corresponding results are presented in Sec. VI before a summary of the measurements in the last section.

II. DATA SETS

The data sets used in this analysis were recorded at RHIC (Brookhaven National Laboratory) during the 2012 and 2013 polarized proton running periods at a center-of-mass

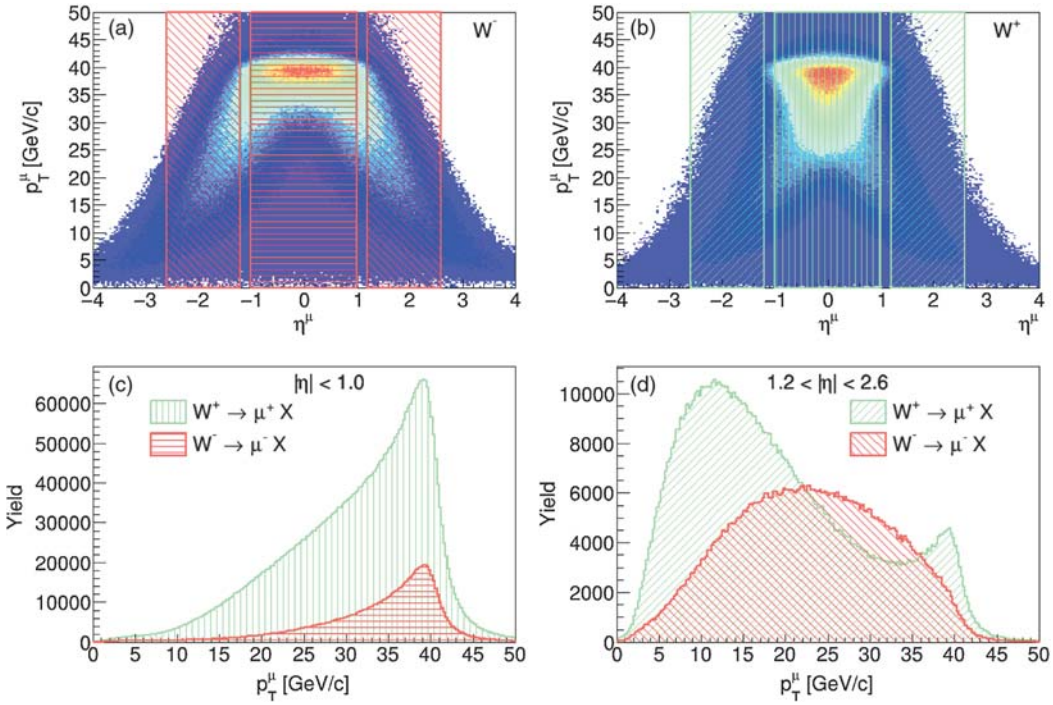


FIG. 1. Two-dimensional rapidity-transverse-momentum distributions for (a) $W^- \rightarrow \mu^-$ decays and (b) $W^+ \rightarrow \mu^+$ decays. Muon transverse momentum projected yields for (c) central rapidities ($|\eta| < 1$) and (d) forward rapidities ($1.2 < |\eta| < 2.6$). The positive decay muons are displayed in the (c) vertical and in the (d) $+45^\circ$ from vertical (green) hatched regions, while the negative decay muons are displayed in the (c) horizontal and in the (d) -45° from vertical (red) regions.

energy $\sqrt{s} = 510$ GeV. A luminosity of approximately 53 and 285 pb^{-1} sampled within a wide vertex region of about 40 cm width was used for this analysis for the two running periods, accumulated with the PHENIX detector (see Fig. 2). The average beam polarizations were 56% and 58% for the two beams in the 2012 running period and 54% and 55% in the 2013 running period. The polarization

uncertainty was obtained by the RHIC polarimetry group and amounts to a relative 3% per beam. These uncertainties translate into a global normalization uncertainty of the extracted asymmetries.

The $W \rightarrow \mu$ candidate events were detected via tracks in the forward muon arm system [15], which comprises the muon tracker (MuTr) and muon identifier (MuID)

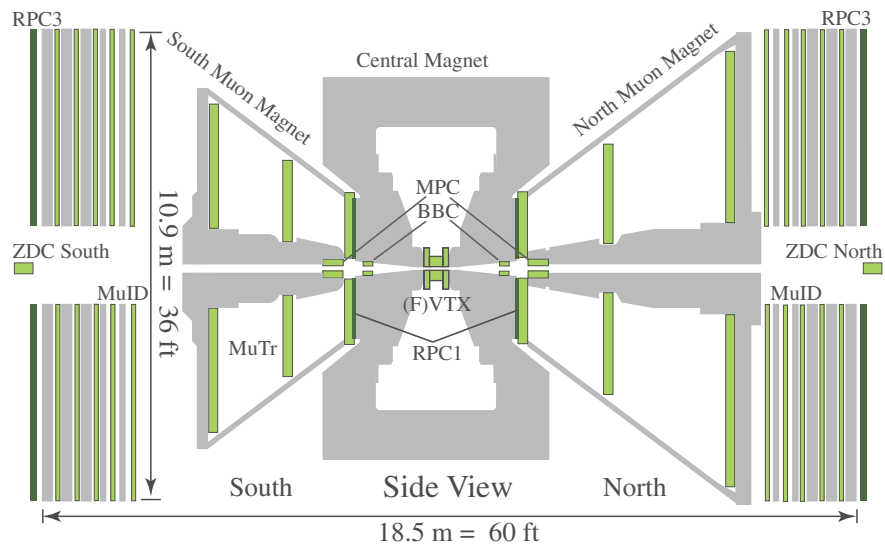


FIG. 2. A side view of the PHENIX detector, concentrating on the muon arm instrumentation. Of primary importance to this analysis are the BBC, FVTX, RPC, MuTr, and MuID. Please see text for descriptions of these subsystems and how they were used.

subsystems. A newly installed set of resistive-plate chamber (RPC) detectors [16] in the muon arms were also used to associate tracks with particular beam crossings and to help with triggering. For tracks traversing the full array of detectors, the full azimuthal acceptance is covered over the region $1.1 < |\eta| < 2.5$ and $1.1 < |\eta| < 2.6$ in the two arms, respectively. However, the range of vertex longitudinal positions is reduced at the boundaries of the η coverage. The collision vertex was determined by the PHENIX beam-beam counters (BBC), which are two sets of 64 Čerenkov counters with a pseudorapidity range of $3.0 < |\eta| < 3.9$.

Prior to these data sets, no momentum selectivity was available for triggering forward muons in PHENIX; only an enhancement of real muons (rejection of fake tracks) was available based on the activity in the downstream MuID planes. To enhance the W data sample within the limited bandwidth available, the forward PHENIX detectors were upgraded to allow triggering on all $W \rightarrow \mu$ candidates. New readout electronics for the MuTr (MuTrig) [17] were added, and the RPCs were installed upstream and downstream of the muon arms. In both subsystems, the azimuthal segmentation allowed for the selection of events with muon candidates traversing the whole muon system and with nearly straight lines in real time. Depending on the polar angular coverage of the RPCs, three main types of triggers were created. At low pseudorapidities ($|\eta| < 1.4$), only the upstream RPCs were in coincidence with the MuTrig and collision counters, while at high pseudorapidities ($|\eta| > 2.0$), only the downstream RPCs were available for coincidence with the MuTrig and collision counters. In the intermediate region, a coincidence of both RPCs and the MuTrig was required. This new trigger selected track candidates that satisfied a minimum momentum threshold of approximately 10 GeV/*c*.

Several other trigger combinations less sensitive to momentum were considered at reduced data taking rates for this analysis, in addition to the main triggers described above. In 2012 only the downstream RPCs were part of the trigger while the upstream RPCs were only used in the off-line analysis. For triggers without downstream RPC information a coincidence with a hit in the furthest plane of the MuID is required, enforcing the track candidate to penetrate at least $12.8 \lambda_I$ ($1.1 < \eta < 2.6$) and $12.0 \lambda_I$ ($-2.4 < \eta < -1.1$) nuclear interaction lengths. For a trigger cross-check and efficiency evaluation, independent data samples were collected which only relied on the muon identifier or entirely different PHENIX detector components.

As the data collision rate far exceeded the capacity of the PHENIX data acquisition system to record data, only a small fraction (1 in every 30 to 130 events, depending on luminosity) of this data was written to tape for further analysis, while for the new momentum-sensitive triggers, essentially all events were recorded. The total trigger efficiencies for W -decay muon candidate events varied

as a function of rapidity due to the combination of different trigger components according to their individual ranges of coverage. For example, at very low (high) rapidities, only upstream (downstream) RPCs were available, which reduced their rejection rates but increased the trigger efficiencies in these regions. These trigger efficiencies are summarized in Fig. 3 for positive and negative muons at forward and backward rapidities, showing the discussed rapidity dependence for the 2013 data taking period. In the 2012 running period, the upstream RPCs were still being commissioned, and simpler triggers using mostly the MuTrig information, the MuID, and the downstream RPCs were used. As such, the rapidity range was more limited, but the efficiencies were nearly constant over that range (approximately 50% to 60% for the two arms and charges).

Moreover, in the 2012 and 2013 running periods, a new forward vertex detector (FVTX) was available [18], consisting of four planes of silicon strips finely segmented in radius and coarsely segmented in azimuth. For the subset of muon candidate tracks passing several of these detector planes (about 10%–30% of tracks), this additional information was used to improve tracking quality and to further reduce jetlike events.

During collider downtime and periods prior to and after the end of the 2011–2013 physics runs, cosmic-ray data were collected. The rate of high-energy cosmic-ray muons in the PHENIX detector—as a potential background to the

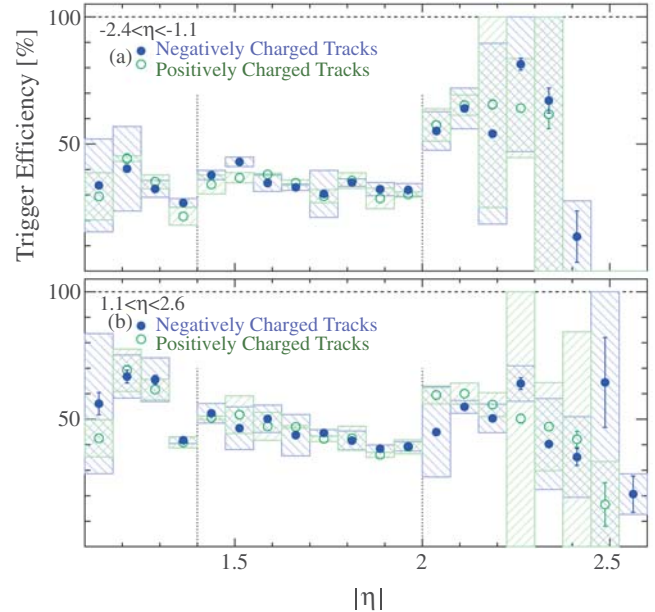


FIG. 3. Trigger efficiencies for the 2013 running period as a function of η for negative (blue solid circles) and positive (green open circles) W decay muon candidates in (a) south and (b) north PHENIX muon detector arms for pseudorapidity ranges (a) $-2.4 < \eta < -1.1$ and (b) $1.1 < \eta < 2.6$. The hatched boxes correspond to the systematic uncertainties in the trigger efficiency calculations. The vertical, dotted lines represent the approximate boundaries of the three main RPC-based triggers.

W signal—was found to be negligible (below 1% of the expected W decay muons) when applying the same selection criteria as for W decay signal candidates. This large sample of cosmic-ray events provides crucial information on the reconstruction performance of the muon arms for high-momentum tracks. Muons traversing both spectrometer arms are reconstructed as a pair of back-to-back muon tracks that have nearly the same momenta but opposite charge signs. Incoming tracks enter the spectrometer arm from outside the detector volume, pass through the detector, and exit through the opposite spectrometer. They are also required to pass the nominal vertex region, which, together with the two-arm requirements, limits their η acceptance in comparison to the W analysis.

Using these data, the charge sign reconstruction efficiencies were investigated. Owing to the limitations in the spectrometer segmentation, measuring the bend plane becomes ambiguous for the highest momentum tracks, which are almost straight. The rate of each incoming charge sign is compared to the rate of oppositely charged outgoing muons. The difference is an inefficiency in the charge sign reconstruction. The results of this test are shown in Fig. 4. As expected, the charge sign reconstruction is $\sim 100\%$ for low momentum tracks and is $\sim 90\%$ ($\sim 80\%$) for the spectrometer located at $1.1 < \eta < 2.6$ ($-2.5 < \eta < -1.1$) at high momenta. These results are found to be well reproduced in simulations.

Direct comparison of the reconstructed momentum from the incoming and outgoing part of each cosmic muon track indicates the accuracy of the momentum reconstruction.

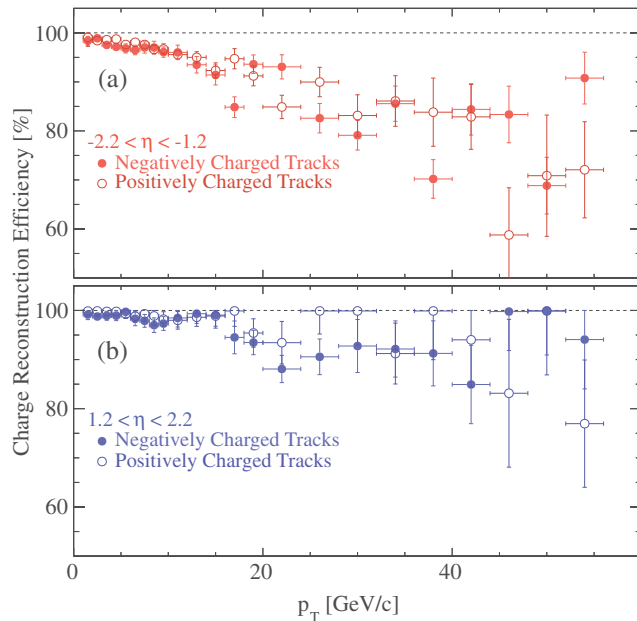


FIG. 4. Charge-sign reconstruction efficiency for the (a) south and (b) north muon arms. The (a) $-2.2 < \eta < -1.2$ (red) and (b) $1.2 < \eta < 2.2$ (blue) solid and open circles are for negatively and positively charged tracks, respectively.

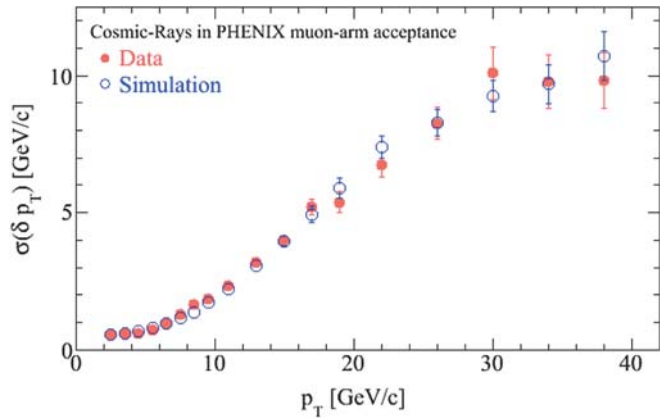


FIG. 5. Momentum reconstruction resolution from measured (red solid circles) and simulated (blue open circles) cosmic-ray muons.

Figure 5 shows the relative (between arms) resolution of the transverse momentum reconstruction for cosmic data and simulation. Although the accuracy is low for high-momentum tracks ($\sigma \sim 25\%$), this is well reproduced in the simulations, indicating that the data will be accurately imitated by the simulations. The variation of this momentum reconstruction accuracy in simulations will be considered as uncertainties due to detector smearing. An additional rate-dependent degradation in the momentum smearing was taken into account in the corresponding simulations.

In addition to the collected physics data sample, several sets of Monte Carlo (MC) simulated data were produced and analyzed. First, a large sample of PYTHIA+GEANT3 [19] simulations was used to estimate the reconstruction efficiency for high-momentum muons representing the W signal. In addition, RHICBOS [20] and CHE [21] were used as generators for signal events. Muonic decays of Z boson production were included in the signal simulations as they are indistinguishable in this analysis. To ensure that the MC data represent the collected data, residuals between hits and reconstructed tracks and other kinematic distributions were compared to pure muon samples collected from cosmic-ray and positively identified muons (from J/ψ decays). The MC distributions were found to reproduce those in data accurately.

Similar large scale PYTHIA+GEANT simulations were also performed for various background contributions. Heavy flavor decays into muons as well as muonic decays of charmonium and bottomonium resonances dilute the W decay muon signal as they are indistinguishable from real W boson decay muons. Due to the sizable momentum smearing at high reconstructed transverse momenta, these decays do contribute substantially even though their actual transverse momenta drop rapidly. To ensure that these simulated single muon background contributions correctly describe the real muon background, their relative

contributions were evaluated using fits to opposite sign dimuon invariant mass data. The weighted simulated real muon background contributions were then fixed in the W signal fits of the single muon candidates, while the individual weights' correlated uncertainties were assigned as systematic uncertainties.

Another suite of MC data probed the contribution of background particles that may masquerade as W decay muons. This comprises contributions from π^\pm and K^\pm decays. Single π^\pm and K^\pm +GEANT simulations are used to estimate the fake background from in-flight decays within the muon spectrometer. Their generated contributions are weighted based on next-to-leading order (NLO) calculations [22] in the same rapidity range. They are consistent with the available experimental data, as well as PYTHIA TuneA simulations that generally reproduce hadronic cross sections at RHIC energies. Due to their large initial cross section, especially at low transverse momenta, a sizable contribution of hadrons survive all absorbing material upstream of the muon tracker, and their subsequent decays may appear as near-straight tracks and get misreconstructed as high-momentum tracks. A substantial part, more than 98%, of such fake muons can be rejected due to the large amount of multiple scattering in the absorbing matter and thus poorer correlations between different detector systems. However, not all such candidates can be removed, leaving these as the most important background in the W measurements. The majority of effort in this analysis concentrates on reducing this hadronic background, ensuring its reliability from the simulations to the data and fitting its contributions in the signal enhanced data sample.

III. EVENT AND TRACK SELECTION CRITERIA

The triggered data sample was further analyzed to reduce contamination of nonmuon particles in the sample. A candidate muon was formed from two pieces of information: a formed track in the muon spectrometer and a short “road” through the whole of the MuID. Muonlike track quality was determined through residual distributions of track and road variables that combine to form a powerful method to distinguish real and fake muons. These residuals can be classified into three broad categories: identification, track/road matching, and physics.

For each high-momentum track candidate ($16 \text{ GeV}/c < p_T < 60 \text{ GeV}/c$) in the spectrometer ($1.1 < |\eta| < 2.6$), the difference between the measured hit positions of the track and the subsequent fit are used to form a χ^2 per degree of freedom residual. This track- χ^2 residual, coupled with the requirement that the track passes through the whole MuID, establishes tracks as muon candidates.

The second category, track/road matching, is an ensemble of variables that are sensitive to differences between real muons and fake-muon backgrounds formed from the decay

of light hadrons (particularly K^\pm) within the volume of the muon spectrometer. Such decays produce a kink in their track, changing the trajectory measured in the spectrometer relative to that in the MuID. Therefore, the angular and spatial differences between the track and the road of the candidate are wider for hadron-decay muons than for muons originating at the collision vertex. Also, the distribution of the projections to the collision vertex is broader due to the multiple scattering in the absorbing materials. These decay hadrons have two properties. First, these are typically low-momentum hadrons that have punched through the central arm magnet return yoke ($4.9 \lambda_I$ steel) and absorber ($2.3 \lambda_I$ steel) nuclear interaction lengths. Second, the decay kinematics for some of these hadrons result in a mismeasurement of the track momentum, promoting the originally low momentum particle to higher momenta. Although there is only a tiny probability of this confluence, the large number of light hadrons produced in soft $p + p$ interactions makes this the dominant source of fake-muon background in this analysis.

The final track residual category utilizes the newly installed RPC detectors to associate tracks with particular beam crossings. Typically 107 to 111 of 120 bunches were filled during these running periods with bunch crossings every 106 ns. The RHIC accelerator provides alternating orientation of the proton polarization in two groups of four combinations. This alternating approach minimizes systematic effects of individual bunch crossings' varying beam luminosity and polarization. As a consequence, specific tracks have to be matched in time to particular beam crossings. The RPCs provide a space-time stamp for each candidate track, whereby the spatial information is used to assign an RPC cluster to the track, and the corresponding time is used to identify the correct beam crossing. A tight requirement is imposed on the distance of closest approach (between the RPC cluster and the projected track trajectory onto the RPC plane), along with a stringent time window to reject tracks from prior/subsequent crossings.

Finally, the matching of the fully formed muon candidate to the collision vertex position (estimated using the BBC) rejects background tracks that do not originate at the point of collision. For data taking in 2013, the RPCs and their matching information were already implemented as part of the main trigger while for 2012 this matching needed to be performed off-line for the upstream RPCs.

For the FVTX detector, similar matching variables were used if several FVTX planes were hit and formed a FVTX track candidate. Additionally, for each track in the muon arms, the number of FVTX track candidates in the vicinity is counted. This provides additional information to suppress both heavy flavor and fake muon backgrounds because their muon candidate tracks are more likely found within a jet of particles.

For each event, the value of each track residual is given a probability based on reference distributions from simulated

W decays, λ_{Sig} , and collected data, λ_{Bg} . The latter is effectively a background distribution due to the low percentage of signal present (<0.1%). The use of the full data distribution for the background allows for the correct mixing of hadronic and muon backgrounds. A combined probability distribution,

$$W_{\text{ness}} = \frac{\lambda_{\text{Sig}}}{\lambda_{\text{Sig}} + \lambda_{\text{Bg}}}, \quad (3)$$

is formed from all variables available, including track and road matching position and angular residuals, transverse distance to the vertex point, residuals to the RPC clusters, FVTX matching residuals, and FVTX track candidate multiplicity. It is displayed in Fig. 6, where probabilities close to unity represent W -muon-like tracks, while near zero probabilities represent hadronic background dominated events. Tracks with high W_{ness} (>0.92) are used for further analysis. This value was chosen as a compromise between signal purity (around 10% to 17%) and efficiency (above 95%) to optimize the uncertainties of the background corrected asymmetries. The W_{ness} data distribution is reasonably well described by a combination of the individual MC simulations for the signal, real muon, and hadronic backgrounds.

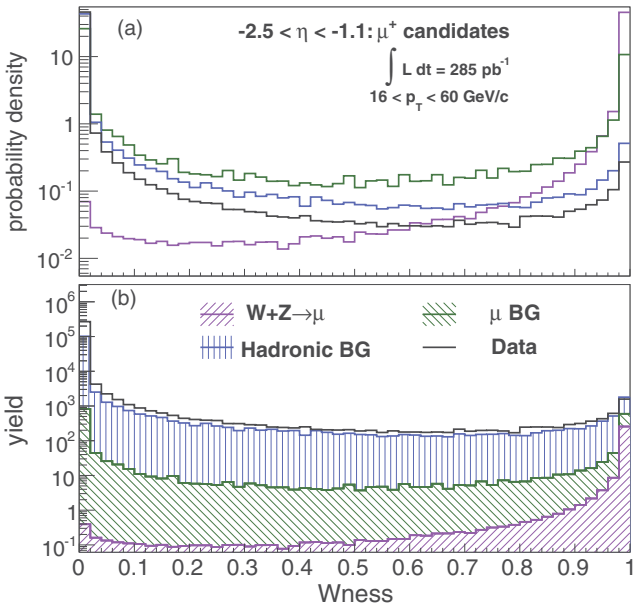


FIG. 6. (a) Probability density distribution for W_{ness} and (b) absolute yields of data and stacked simulated signal and background contributions as a function of W_{ness} . (a) The sequence of curves from top to bottom for $W_{\text{ness}} < 0.6$ is muon background (dark green line), hadronic background (blue line), data (black line), and simulated signal (purple line). (b) The sequence of curves and shadings from top to bottom is data (black line), hadronic background (blue area), muon background (green area), and simulated signal (purple area).

TABLE I. Kinematic variables used in the W_{ness} evaluation. Variables in square brackets were not available for all events due to the different acceptances of the respective subsystems.

Variable	Description
DG0	track-road difference at first MuID plane's z position
DDG0	track-road angular difference at first MuID plane's z position
DCA _r	radial distance of extrapolated track at vertex z position
FVTX N_{clus}	FVTX track multiplicity in cone around extrapolated track candidate
RPC1 _{DCA}	[RPC1 hit cluster-track difference at RPC1 z position]
RPC3 _{DCA}	[RPC3 hit cluster-road difference at RPC3 z position]
FVTX $\Delta\phi, \Delta r, \Delta\theta$	[FVTX track and MuTr residuals] and $\Delta\theta$

As not all detector components (upstream, downstream RPCs, and FVTX detectors) cover the whole rapidity range, between five to nine kinematic and residual variables entered the combined probability. For correlated variables, the initial probability density functions were evaluated together. The different variables are summarized in Table I.

IV. SIGNAL EXTRACTION AND BACKGROUNDS

After selecting candidate tracks as muon candidates, most of the remaining tracks are still not muons from W decays. An unbinned maximum likelihood fit approach is used to determine the final number of W 's and remaining backgrounds. Figure 7 illustrates the two discriminant variables used to normalize the relative contribution of the signal and backgrounds. Figure 7(a) shows the pseudorapidity of the track for data (solid circles) along with the expected distributions from signal muons (purple solid line), background muons (green solid line), and the residual misidentified hadronic background (blue solid line). Figure 7(b) shows a variable determined from the azimuthal bend plane between the second and third muon spectrometer stations, $dw_{23} = \Delta\phi_{23} \times \sin\theta \times p_T$, where $\Delta\phi_{23}$ is the difference of the azimuthal angle between the second and third station hits and θ is the polar angle of the track relative to the beam direction. The pseudorapidity and dw_{23} variables are found to be almost orthogonal in sensitivity.

The underlying discriminant shapes for the signal W muons and real muon backgrounds are determined from the MC simulations. The normalization (for the muon backgrounds) is determined from the yield of c, b , and quarkonia decays in PYTHIA as evaluated via fits to the dimuon data. For the hadronic background shape, the azimuthal bend-plane distributions were extracted from hadron simulations directly in the target W_{ness} region ($W_{\text{ness}} > 0.92$) as no unbiased hadronic background only data sample was available. The pseudorapidity variable is

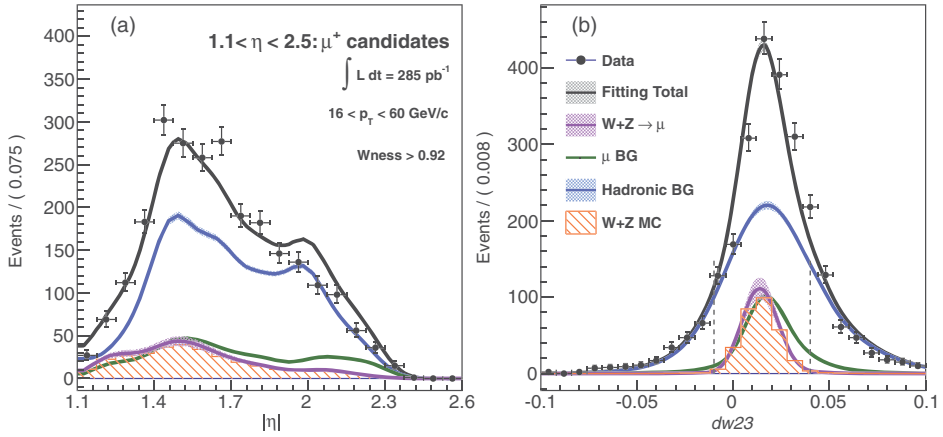


FIG. 7. Signal and background discrimination of positive rapidity μ^+ candidates. (a) Pseudorapidity and (b) azimuthal bend-plane-variable, dw_{23} , dependence from top to bottom for data points, curves, and hatching for (a) $|\eta| = 1.6\text{--}2.3$ and (b) $dw_{23} = 0.024\text{--}0.04$ are data (black solid circles), combined fitting total (black curve), hadronic background (blue curve), real-muon background (dark green curve), signal (purple curve), and MC-based expected-signal yields (red hatched area). The relative yields of signal and backgrounds are determined from a simultaneous fit to both discriminant distributions. The additional azimuthal bend-plane variable range selection for the asymmetry evaluation is shown as vertical dashed lines.

extracted from data in the target W_{ness} region from the sidebands of the azimuthal bend-plane variable where neither signal nor background muons contribute. It corresponds to $dw_{23} < -0.05(-0.01)$ or $dw_{23} > 0.01(0.05)$ for negative (positive) tracks, respectively. Final signal-to-background ratios vary from 10% to 17%, depending on charge sign and spectrometer arm before restricting the azimuthal bend-plane variable for the asymmetry analysis. To obtain the corresponding cross sections, the extracted signal yields get corrected for charge misidentification (<2%), reconstruction and acceptance efficiencies (approximately 0.6% for W^+ and 2% for W^-), trigger efficiencies, and Z boson admixture (18% to 22%). The yields are then normalized by the accumulated luminosity to arrive at the $W \rightarrow \mu$ cross sections.

To extract the single spin asymmetries, the high W_{ness} ($W_{\text{ness}} > 0.92$) data sample was taken with the additional selection of the azimuthal bend-plane variable with W support only (± 0.01 to ± 0.04 , for positive and negative charges, respectively) and rapidities $\eta < 2$. In this region, the signal-to-background ratios increase to between 15% and 28%. The yields were separated according to the helicity combinations normalized by the corresponding beam polarizations. For each arm and charge, a single spin asymmetry for each beam and a combined double spin asymmetry can be extracted. The differences in relative luminosity were accounted for by using scalers from the PHENIX collision counters as relative weights. The uncertainties on these correction factors are insignificant relative to the other uncertainties. No background process should possess a parity-violating asymmetry. This was experimentally verified by either selecting muon candidates at lower transverse momenta or lower W_{ness} . Consequently, the actual $W + Z$ single spin asymmetries can be extracted

from the raw asymmetries by correcting the dilution from the background using the obtained signal-to-background ratios. Because the signal-to-background ratios are still well below unity, the variation of the background correction, according to the uncertainties on the signal-to-background ratios, results in large systematic uncertainties on the asymmetries, which are comparable to the statistical uncertainties.

V. SYSTEMATIC STUDIES

To estimate the systematic uncertainties on the signal-to-background ratios, several factors impacting them have been varied. The most important factor involves the amount of real muon backgrounds because that contribution was fixed in the unbinned maximum likelihood fits. As real muon backgrounds most closely resemble the rapidity and azimuthal bend-plane distribution of the signal, a smaller/larger muon background weight gets preferentially compensated with a larger/smaller signal yield. To evaluate these uncertainties, the amount of muon backgrounds was varied according to the uncertainties obtained on the individual weights of the various charm and bottom contributions in the dimuon fits. As some of these values are correlated, the calculated correlation matrix was fully taken into account when varying these contributions. Another uncertainty originates from varying the trigger efficiency, which affects the real muon backgrounds, as well as the total reconstruction efficiencies for the cross section measurements. While the effect of varying the trigger efficiencies according to their uncertainties is small, in the reconstruction efficiency correction, it again enters the signal-to-background fits via the size of the muon backgrounds. The trigger efficiencies were varied

TABLE II. $W \rightarrow \mu^\pm$ cross section systematic table for the 2013 data in pb. The uncertainties of the 2012 data set are comparable. The individual contributions and their asymmetric lower and upper systematic uncertainties, denoted as lower and upper, are given for each charge and arm.

Systematic	South muon arm				North muon arm			
	$W^- \rightarrow \mu^-$		$W^+ \rightarrow \mu^+$		$W^- \rightarrow \mu^-$		$W^+ \rightarrow \mu^+$	
	Lower	Upper	Lower	Upper	Lower	Upper	Lower	Upper
Smearing	4.12	2.48	14.67	11.16	1.65	1.87	5.89	7.90
μ BG	13.60	13.71	33.82	33.80	11.51	11.66	24.76	24.87
MC checks	4.06	0.00	18.22	0.00	11.23	0.00	12.94	0.00
Trigger efficiencies	2.37	0.56	4.63	4.11	1.81	1.59	2.93	2.73
Luminosity scale	0.09	0.07	6.53	8.00	1.51	1.85	4.64	5.67
Charge reconstruction efficiency	9.67	0.31	1.04	31.59	0.08	6.00	18.43	0.28
Z admixture	1.50	0.00	0.04	0.00	2.32	0.00	0.41	0.00
Acceptance	1.83	4.44	8.93	21.91	2.31	3.26	5.63	9.92

according to their statistical and systematic uncertainties. The latter originates from different ways of extrapolating the trigger efficiencies to the high W_{ness} region, as well as from the use of different reference data samples to obtain the trigger efficiencies. Another uncertainty affecting the real muon backgrounds, as well as the total cross section, is the uncertainty on the accumulated luminosity. A dedicated analysis using van der Meer scans to obtain the total cross sections for the luminosity detectors in PHENIX determined the systematic uncertainty to be 10%. The luminosity has been varied accordingly in fit and cross section calculation to obtain the corresponding uncertainty. The correctness of the signal extraction procedure is tested in fully MC simulated data. While generally found reliable, a tendency of the hadron background shape extraction to cause the signal to be overestimated in the fits was found. As a consequence, a systematic uncertainty is assigned according to the relative overestimation seen in these fully simulated MC fits. Additional uncertainties are obtained by varying the momentum smearing in the signal and background simulations according to the experimentally found uncertainties.

To obtain cross sections, the extracted yields need to be normalized by the accumulated luminosity and corrected for reconstruction efficiencies and acceptance. For the reconstruction efficiency and acceptance correction two methods were used. Either the signal from PYTHIA events were used to evaluate the correction factor or from the NLO generator RHICBOS [20]. In both cases, the rapidity dependence is quite similar, and the differences were assigned as systematic uncertainties. Also, the dependence on the collision rate has been taken into account. Similarly, we cannot experimentally identify and remove Z boson decays to muons, so we used these two MC generators to remove the Z contributions. These contributions amount to about 18% to 22% for positive and negative muons, respectively. Again, the differences between PYTHIA and RHICBOS were assigned as systematic uncertainties. As was shown in Fig. 4, the charge reconstruction efficiencies are generally

very high and well described by MC simulations. The efficiencies are found to drop toward low absolute pseudorapidities. To estimate its possible effect, the difference from the results with a charge misidentification rate of 20% was assigned as systematic uncertainty. Due to the larger yields for positive muons, this systematic uncertainty results in lower uncertainties on the W^- and upper uncertainties on the W^+ cross sections.

All these contributions were varied either in the unbinned maximum likelihood fits directly or in the cross section extractions. The individual uncertainties were assumed to be uncorrelated, and a Gaussian sampling technique was applied to obtain the total uncertainties on the signal-to-background ratios as well as for the cross sections. For the asymmetry calculations the uncertainties on the signal-to-background ratios as well as the impact of charge misidentification and smearing were again taken into account in the background-corrected asymmetries. The systematic uncertainties of the cross section measurements are summarized in Table II.

Apart from these contributions to the systematic uncertainties, various consistency checks were performed to ensure that signals are reliably extracted and the single spin asymmetries are correct. The asymmetries were tested with randomized helicity patterns to ensure that no false asymmetries and no hidden systematic uncertainties were present. When changing either the momentum range or the W_{ness} range, the number of background events rapidly grows and the asymmetries all become consistent with zero as expected.

VI. RESULTS

Figure 8 shows the extracted total cross sections for inclusive $W^\pm \rightarrow \mu^\pm$ production in $p + p$ collisions at a center-of-mass energy of 510 GeV. The cross sections are consistent within uncertainties with previous measurements at this energy from central $W \rightarrow e$ decay channels [12,23] and with the expected NLO predictions. The uncertainties

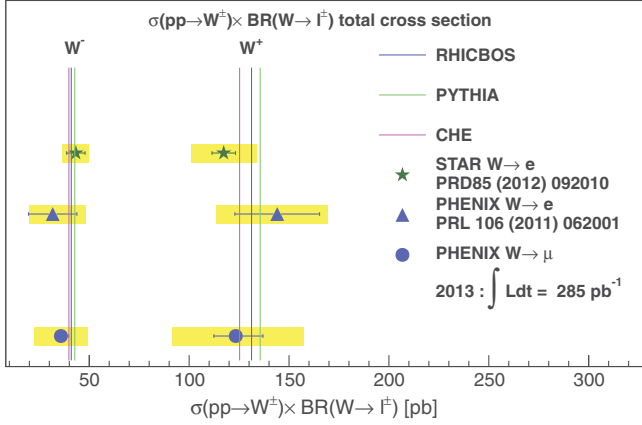


FIG. 8. The $W^\pm \rightarrow \mu^\pm \nu$ cross section measured at forward and backward rapidity from this measurement averaged over both arms $1.1 < |\eta| < 2.5$ (blue solid circles) and central rapidity measurements from PHENIX– $-0.35 < \eta < 0.35$ (blue solid triangles) [13] and STAR– $-1.0 < \eta < 1.0$ (green solid stars) [11]. The horizontal bars and yellow shading show the statistical and systematic uncertainties, respectively. The vertical-line estimates from the NLO generators are from left to right CHE (purple line), RHICBOS (blue line), and PYTHIA6.4, using TuneA and a k -factor of 1.4 (green line).

are dominated by the large uncertainty on the extracted signal-to-background ratios but are comparable with the previously published PHENIX results at central rapidities.

The longitudinal single-spin asymmetries, A_L , measured at forward and backward rapidities are shown in Fig. 9(a) for positive and Fig. 9(b) for negative $W + Z$ decay muon candidates. The two individual single spin asymmetries from the two colliding beams have been combined after correcting for background. Vertical lines and boxes show the statistical and systematic uncertainties, respectively. The curves depict parametrizations for the quark and antiquark helicity PDFs based on various global fits [24–27] as evaluated for the $W + Z \rightarrow \mu$ process at NLO in the strong coupling using the CHE generator [21].

For the NNPDFpol1.1 set, the uncertainty bands based on their 100 replicas are also displayed in Fig. 9. At forward μ^- rapidities, the DSSV08 curves for two scenarios in which $\Delta d(x)/d(x)$ approaches unity when x is approaching unity are also displayed for comparison. The previously published central $W(+Z) \rightarrow e$ asymmetries from the STAR experiment [11] and PHENIX [13] are also shown. The 2013 results from STAR are still expected [28].

These asymmetries show the first muon single spin asymmetry results from $W + Z$ decays at pseudorapidities $|\eta| > 1$ of the decay lepton. They help determine the valence and sea quark helicities at different momentum fractions than at central rapidities. The uncertainties are substantial due to the large systematics on the signal extraction and the relatively small signal fractions in the selected data sample. The behavior of the asymmetries is generally consistent with the parametrizations although the forward μ^- asymmetry is

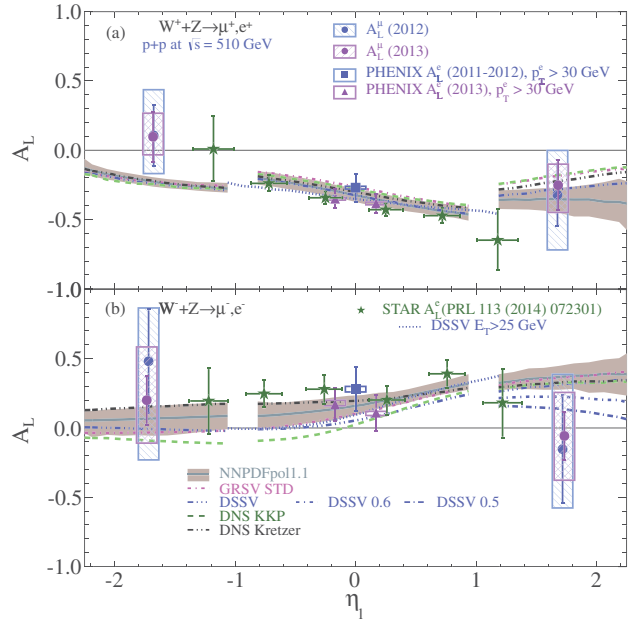


FIG. 9. Longitudinal single spin asymmetry, A_L for (a) $W^+ + Z \rightarrow \mu^+, e^+$ and (b) $W^- + Z \rightarrow \mu^-, e^-$. The PHENIX results are for the current combined two muon arms for 2012 (blue solid circles) and 2013 (purple solid circles), $p_T^\mu > 16$ GeV, and for previously published 2010 + 2012, $p_T^e > 30$ GeV (blue solid squares), and 2013, $p_T^e > 30$ GeV (purple solid triangles) [13]. The STAR results (green solid stars) [11] are for combined 2011 + 2012. Also shown are the statistical error bars and systematic uncertainty boxes. The curves depict helicity PDF parametrizations from various global fits described in the text that are calculated using the polarized NLO generator CHE.

below the DSSV08 curve. While the predicted asymmetries, including a scenario where the d -quark polarization changes sign and becomes positive at very large x ($x > 0.5$), are more compatible with this result, the precision is not sufficient to actually confirm it. The backward μ^- asymmetries are at the upper limit of the uncertainty bands, which is similar to the central measurements and indicates a $\Delta \bar{u}(x)$ larger than the central values obtained in the global fits without the RHIC W measurements. The forward μ^+ asymmetries are in agreement with the parametrizations, while the backward asymmetries prefer substantially smaller asymmetries. Based on the helicity parametrizations, the asymmetries are dominated by the well-known up-quark helicities. The relatively small NNPDF uncertainty band is dominated by the antidown quark helicity uncertainties. However, for W^+ production at forward rapidities and our transverse momentum selection, there is always a mixture of up and antidown flavors from either proton that contributes at a rather different x . It is possible that a higher unpolarized antidown quark component reduces the size of the asymmetries. Such uncertainties in the unpolarized PDFs are not included in the uncertainty bands of the asymmetry parametrizations. This larger unpolarized contribution could explain our surprisingly small backward W^+ asymmetries.

TABLE III. Single-spin asymmetries at forward A_L^{FW} and backward A_L^{BW} rapidities for $p + p$ collisions at $\sqrt{s} = 510$ GeV for results in 2013 and 2012, plus combined results for both years.

Year	$A_L^{FW}(W^+ + Z \rightarrow \mu^+)$	$A_L^{BW}(W^+ + Z \rightarrow \mu^+)$	$A_L^{FW}(W^- + Z \rightarrow \mu^-)$	$A_L^{BW}(W^- + Z \rightarrow \mu^-)$
2013	$-0.252 \pm 0.18(\text{stat})^{+0.18}_{-0.24}(\text{syst})$	$0.097 \pm 0.18(\text{stat})^{+0.21}_{-0.16}(\text{syst})$	$-0.057 \pm 0.18(\text{stat})^{+0.31}_{-0.32}(\text{syst})$	$0.201 \pm 0.18(\text{stat})^{+0.38}_{-0.31}(\text{syst})$
2012	$-0.321 \pm 0.22(\text{stat})^{+0.28}_{-0.36}(\text{syst})$	$0.107 \pm 0.22(\text{stat})^{+0.29}_{-0.24}(\text{syst})$	$-0.153 \pm 0.39(\text{stat})^{+0.53}_{-0.44}(\text{syst})$	$0.481 \pm 0.37(\text{stat})^{+0.41}_{-0.65}(\text{syst})$
Both	$-0.283 \pm 0.14(\text{stat})^{+0.23}_{-0.29}(\text{syst})$	$0.102 \pm 0.14(\text{stat})^{+0.24}_{-0.20}(\text{syst})$	$-0.087 \pm 0.16(\text{stat})^{+0.38}_{-0.35}(\text{syst})$	$0.291 \pm 0.16(\text{stat})^{+0.38}_{-0.44}(\text{syst})$

The total W boson production cross sections for $p + p$ collisions at $\sqrt{s} = 510$ GeV for $\sigma(W^+ \rightarrow \mu^+)$ and $\sigma(W^- \rightarrow \mu^-)$ are $123.31^{+13}_{-11}(\text{stat})^{+34}_{-31}(\text{syst})$ pb and $35.80^{+3.9}_{-3.0}(\text{stat})^{+13}_{-13}(\text{syst})$ pb, respectively. The corresponding single-spin asymmetries, including their uncertainties, are summarized in Table III.

VII. SUMMARY

In summary, PHENIX has measured the first longitudinally polarized single spin asymmetries in $W \rightarrow \mu$ production at decay lepton pseudorapidities larger than unity. The asymmetries from global fits of previous longitudinally polarized world data are mostly consistent with our results. However, our data also show a tendency for antiup quark helicities to be closer to the upper limit of the previously extracted uncertainties. These measurements will play a major role in reducing the uncertainties in future global helicity fits over a larger x range than previously covered.

ACKNOWLEDGMENTS

We thank the staff of the Collider-Accelerator and Physics Departments at Brookhaven National Laboratory and the staff of the other PHENIX participating institutions for their vital contributions. We also thank D. DeFlorian and E. Nocera for their support in setting up the CHE W simulations with their NNPDFpol inclusion and W. Vogelsang for many insightful discussions since before the actual measurements were recorded and analyzed. We acknowledge support from the Office of Nuclear Physics in the Office of Science of the Department of Energy, the National Science Foundation, Abilene Christian University

Research Council, Research Foundation of SUNY, and Dean of the College of Arts and Sciences, Vanderbilt University (U.S.A), Ministry of Education, Culture, Sports, Science, and Technology and the Japan Society for the Promotion of Science (Japan), Conselho Nacional de Desenvolvimento Científico e Tecnológico and Fundação de Amparo à Pesquisa do Estado de São Paulo (Brazil), Natural Science Foundation of China (People's Republic of China), Croatian Science Foundation and Ministry of Science and Education (Croatia), Ministry of Education, Youth and Sports (Czech Republic), Centre National de la Recherche Scientifique, Commissariat à l'Énergie Atomique, and Institut National de Physique Nucléaire et de Physique des Particules (France), Bundesministerium für Bildung und Forschung, Deutscher Akademischer Austausch Dienst, and Alexander von Humboldt Stiftung (Germany), J. Bolyai Research Scholarship, EFOP, the New National Excellence Program (ÚNKP), NKFIH, and OTKA (Hungary), Department of Atomic Energy and Department of Science and Technology (India), Israel Science Foundation (Israel), Basic Science Research Program through NRF of the Ministry of Education (Korea), Physics Department, Lahore University of Management Sciences (Pakistan), Ministry of Education and Science, Russian Academy of Sciences, Federal Agency of Atomic Energy (Russia), VR and Wallenberg Foundation (Sweden), the U.S. Civilian Research and Development Foundation for the Independent States of the Former Soviet Union, the Hungarian American Enterprise Scholarship Fund, the US-Hungarian Fulbright Foundation, and the US-Israel Binational Science Foundation.

[1] R. D. Ball *et al.* (NNPDF Collaboration), Parton distributions from high-precision collider data, *Eur. Phys. J. C* **77**, 663 (2017).

[2] C. Schmidt, J. Pumplin, D. Stump, and C. P. Yuan, CT14QED parton distribution functions from isolated photon production in deep inelastic scattering, *Phys. Rev. D* **93**, 114015 (2016).

[3] L. A. Harland-Lang, A. D. Martin, P. Motylinski, and R. S. Thorne, Parton distributions in the LHC era: MMHT 2014 PDFs, *Eur. Phys. J. C* **75**, 204 (2015).

[4] W.-C. Chang and J.-C. Peng, Flavor structure of the nucleon sea, *Prog. Part. Nucl. Phys.* **79**, 95 (2014).

[5] L. Adamczyk *et al.* (STAR Collaboration), Precision Measurement of the Longitudinal Double-Spin Asymmetry for

Inclusive Jet Production in Polarized Proton Collisions at $\sqrt{s} = 200$ GeV, *Phys. Rev. Lett.* **115**, 092002 (2015).

[6] A. Adare *et al.* (PHENIX Collaboration), Inclusive cross section and double-helicity asymmetry for π^0 production at midrapidity in $p + p$ collisions at $\sqrt{s} = 510$ GeV, *Phys. Rev. D* **93**, 011501 (2016).

[7] D. de Florian, R. Sassot, M. Stratmann, and W. Vogelsang, Evidence for Polarization of Gluons in the Proton, *Phys. Rev. Lett.* **113**, 012001 (2014).

[8] A. Accardi *et al.*, Electron ion collider: The next QCD frontier—Understanding the glue that binds us all, *arXiv*: 1212.1701.

[9] C. Bourrely and J. Soffer, Parton distributions and parity violating asymmetries in W^\pm and Z production at RHIC, *Phys. Lett. B* **314**, 132 (1993).

[10] K. Adcox *et al.* (PHENIX Collaboration), PHENIX detector overview, *Nucl. Instrum. Methods Phys. Res., Sect. A* **499**, 469 (2003).

[11] L. Adamczyk *et al.* (STAR Collaboration), Measurement of Longitudinal Spin Asymmetries for Weak Boson Production in Polarized Proton-Proton Collisions at RHIC, *Phys. Rev. Lett.* **113**, 072301 (2014).

[12] A. Adare *et al.* (PHENIX Collaboration), Cross Section and Parity Violating Spin Asymmetries of W^\pm Boson Production in Polarized $p + p$ Collisions at $\sqrt{s} = 500$ GeV, *Phys. Rev. Lett.* **106**, 062001 (2011).

[13] A. Adare *et al.* (PHENIX Collaboration), Measurement of parity-violating spin asymmetries in W^\pm production at midrapidity in longitudinally polarized $p + p$ collisions, *Phys. Rev. D* **93**, 051103 (2016).

[14] T. Sjostrand, S. Mrenna, and P. Z. Skands, PYTHIA 6.4 physics and manual, *J. High Energy Phys.* **05** (2006) 026.

[15] H. Akikawa *et al.* (PHENIX Collaboration), PHENIX muon arms, *Nucl. Instrum. Methods Phys. Res., Sect. A* **499**, 537 (2003).

[16] B. Meredith, PHENIX RPC R&D for the fast RPC muon trigger upgrade, *Nucl. Instrum. Methods Phys. Res., Sect. A* **602**, 766 (2009).

[17] S. Adachi *et al.*, Trigger electronics upgrade of PHENIX muon tracker, *Nucl. Instrum. Methods Phys. Res., Sect. A* **703**, 114 (2013).

[18] C. Aidala *et al.*, The PHENIX forward silicon vertex detector, *Nucl. Instrum. Methods Phys. Res., Sect. A* **755**, 44 (2014).

[19] R. Brun, F. Bruyant, F. Carminati, Si. Giani, M. Maire, A. McPherson, G. Patrick, and L. Urban, GEANT Detector Description and Simulation Tool, 1994; CERN Program Library W5013.

[20] P. M. Nadolsky and C. P. Yuan, Single spin asymmetries with weak bosons at RHIC, *Nucl. Phys.* **B666**, 31 (2003).

[21] D. de Florian and W. Vogelsang, Helicity parton distributions from spin asymmetries in W -boson production at RHIC, *Phys. Rev. D* **81**, 094020 (2010).

[22] W. Vogelsang (private communication).

[23] L. Adamczyk *et al.* (STAR Collaboration), Measurement of the $W \rightarrow e\nu$ and $Z/\gamma^* \rightarrow e^+e^-$ production cross sections at mid-rapidity in proton-proton collisions at $\sqrt{s} = 500$ GeV, *Phys. Rev. D* **85**, 092010 (2012).

[24] D. de Florian, R. Sassot, M. Stratmann, and W. Vogelsang, Extraction of spin-dependent parton densities and their uncertainties, *Phys. Rev. D* **80**, 034030 (2009).

[25] E. R. Nocera, R. D. Ball, S. Forte, G. Ridolfi, and J. Rojo (NNPDF Collaboration), A first unbiased global determination of polarized PDFs and their uncertainties, *Nucl. Phys. B* **887**, 276 (2014).

[26] D. de Florian, G. A. Navarro, and R. Sassot, Sea quark and gluon polarization in the nucleon at NLO accuracy, *Phys. Rev. D* **71**, 094018 (2005).

[27] M. Gluck, E. Reya, M. Stratmann, and W. Vogelsang, Models for the polarized parton distributions of the nucleon, *Phys. Rev. D* **63**, 094005 (2001).

[28] Q. Xu (STAR Collaboration), Measurement of longitudinal single-spin asymmetry for W^\pm production in polarized proton + proton collisions at STAR Collaboration, *Proc. Sci.*, DIS20172018 (2018) 226.